Computational and Structural Biotechnology Journal 19 (2021) 6355–6365

COMPUTATIONAL AND STRUCTURAL BIOTECHNOLOGY JOURNAL

journal homepage: www.elsevier.com/locate/csbj

A novel hotspot of gelsolin instability triggers an alternative mechanism of amyloid aggregation

Michela Bollati [a], Luisa Diomede [b], Toni Giorgino [a], Carmina Natale [b], Elisa Fagnani [a], Irene Boniardi [a], Alberto Barbiroli [c], Rebecca Alemani [a], Marten Beeg [b], Marco Gobbi [b], Ana Fakin [d], Eloise Mastrangelo [a], Mario Milani [a], Gianluca Presciuttini [e], Edi Gabellieri [e], Patrizia Cioni [e], Matteo de Rosa [a,*]

[a] Istituto di Biofisica, Consiglio Nazionale delle Ricerche, Milano, Italy
[b] Department of Molecular Biochemistry and Pharmacology, Istituto di Ricerche Farmacologiche Mario Negri IRCCS, Milano, Italy
[c] Dipartimento di Scienze per gli Alimenti, la Nutrizione e l'Ambiente, Università degli Studi di Milano, Milano, Italy
[d] Eye Hospital, University Medical Centre Ljubljana, Ljubljana, Slovenia
[e] Istituto di Biofisica, Consiglio Nazionale delle Ricerche, Pisa, Italy

ARTICLE INFO

Article history:
Received 5 October 2021
Received in revised form 15 November 2021
Accepted 15 November 2021
Available online 19 November 2021

Keywords:
Amyloidosis
C. elegans
Gelsolin
Misfolding
Pathogenic variant

ABSTRACT

Gelsolin comprises six homologous domains, named G1 to G6. Single point substitutions in this protein are responsible for AGel amyloidosis, a hereditary disease causing progressive corneal lattice dystrophy, cutis laxa, and polyneuropathy. Although several different amyloidogenic variants of gelsolin have been identified, only the most common mutants present in the G2 domain have been thoroughly characterized, leading to clarification of the functional mechanism. The molecular events underlying the pathological aggregation of 3 recently identified mutations, namely A551P, E553K and M517R, all localized at the interface between G4 and G5, are here explored for the first time. Structural studies point to destabilization of the interface between G4 and G5 due to three structural determinants: β-strand breaking, steric hindrance and/or charge repulsion, all implying impairment of interdomain contacts. Such rearrangements decrease the temperature and pressure stability of gelsolin but do not alter its susceptibility to furin cleavage, the first event in the canonical aggregation pathway. These variants also have a greater tendency to aggregate in the unproteolysed forms and exhibit higher proteotoxicity in a *C. elegans*-based assay. Our data suggest that aggregation of G4G5 variants follows an alternative, likely proteolysis-independent, pathway.

© 2021 The Author(s). Published by Elsevier B.V. on behalf of Research Network of Computational and Structural Biotechnology. This is an open access article under the CC BY-NC-ND license (http://creativecommons.org/licenses/by-nc-nd/4.0/).

1. Introduction

Gelsolin (GSN) is a multifunctional regulatory protein responsible for the assembly, disassembly and scavenging of actin filaments through its severing and capping activities [1,2]. The protein is organized in six homologous domains (G1-G6), sharing the same GSN-like fold [3], each hosting at least one Ca^{2+}-binding site. In a Ca^{2+}-free environment, the six domains are closely packed together. Calcium binding induces both subtle local and large global conformational changes [3–6], where actin binding surfaces of G2, G1 and G4 become exposed to solvent. The crystal structure of the activated C-terminal half of GSN with or without actin [4,7] has a structurally conserved G4:G5 interface, suggesting that the interaction between the two domains is relevant for the inactive as well as the activated conformations of the protein.

Single point mutations of *GSN* gene are responsible for a systemic form of amyloidosis called Familial Amyloidosis Finnish type (FAF), also known as AGel amyloidosis (AGel). This autosomal dominant disease, first reported by Jouko Meretoja in 1969 [8], causes progressive deposition of amyloid fibrils in different organs and tissues [9–16]. Currently there is no pharmacological treatment blocking or slowing any form of AGel, and only symptomatic treatments are offered to improve the overall quality of life. AGel patients accept several surgeries, transplants and other invasive and expensive medical procedures, which, however, do not remove the source of toxicity [17,18].

Abbreviations: GSN, gelsolin; AGel, gelsolin amyloidosis.

* Corresponding author.
E-mail address: matteo.derosa@ibf.cnr.it (M. de Rosa).

https://doi.org/10.1016/j.csbj.2021.11.025
2001-0370/© 2021 The Author(s). Published by Elsevier B.V. on behalf of Research Network of Computational and Structural Biotechnology.
This is an open access article under the CC BY-NC-ND license (http://creativecommons.org/licenses/by-nc-nd/4.0/).

The most common forms of AGel are caused by substitutions in G2, including D187N/Y mutations which result in systemic progressive deposition of amyloids [9,10], and N184K and G167R mutations, associated with kidney-localized aggregates [19–21]. The molecular mechanisms underlying D187N/Y and N184K amyloidosis are well understood. These substitutions compromise the G2 calcium binding site, leading to overall destabilization of the domain [6,22–24], with exposure of an otherwise buried peptide, which is aberrantly cleaved by furin in the Golgi [25]. The major product of furin activity, the C68 fragment, becomes a substrate of matrix metalloproteinases (MPP) and the proteolytic cascade eventually leads to the production of two aggregation-prone peptides of 5 and 8 kDa [26].

The mechanism of G167R aggregation instead still needs to be fully elucidated. Although this variant shows local destabilization and susceptibility to furin proteolysis similar to the others, this mutation also promotes domain-swapped oligomerization of the protein [27–29].

Several novel pathological variants have now been reported [30–35], and A551P, E553K, and M517R cluster at the interface between G4 and G5. Little is known about the pathological mechanisms underlying these recently-identified AGel forms. As furin is a sequence-specific protease, G4 and G5 domains do not harbor any putative site potentially recognized by this protease.

Possible furin-alternative processes have been suggested for a sporadic form of AGel associated with the deposition of wild-type (WT) GSN, which is resistant to furin proteolysis [36]. *Ex vivo* mass spectrometry of amyloid deposits from AGel patients carrying the G167R [20], A551P [30,37] and unidentified mutations [19] revealed fragments not corresponding to the 5 and 8 kDa product of furin and MMP proteolysis. It is not yet known whether these peptides originate from alternative proteolytic patterns or from the fragmentation of full-length GSN during the analysis.

The three novel pathological variants, A551P, E553K and M517R, are ideal candidate systems to cast light on alternative amyloidogenic pathways. While awaiting more clinical and histopathological findings to reveal the nature of the aggregated material, we here present a molecular profiling of the variants, evaluating their folding stability, aggregation and protetoxic potential and the impact of the substitutions on structure and dynamics of the protein.

2. Results

2.1. G4:G5 variants do not boost GSN susceptibility to furin or impair its physiological activity

All the amyloidogenic GSN variants characterized so far in domain G2 had increased susceptibility to furin-dependent proteolysis *in vitro* [24,27,28,38]. To investigate whether A551P, E553K and M517R substitutions affect the proteolysis, we first examined their sensitivity to furin, using the WT and D187N GSN as controls. As expected, only the D187N variant produced a significant amount of the C68 fragment, the larger product of furin proteolysis. Two additional faint bands were also observed for all variants. These bands previously reported in similar experiments were interpreted as a product of unspecific proteolysis [24] (Fig. S1).

The PROSPER algorithm, a machine learning-based predictor of protease cleavage sites, excluded that the single point substitutions of A551, E553 and M517 could generate novel protease cleavage sites [39].

We tested whether the mutations affect GSN's physiological function, i.e. its ability to bind and sever actin filaments in a pyrene-labeled fluorometric assay. Under Ca^{2+}-free conditions, where GSN adopts the closed and compact conformation, actin binding and severing activity were negligible (0.62 ± 0.01 h^{-1} for WT) and no pathological mutant analysed so far behaved differently [4,28]. The same was true for the A551P and M517R variants (respectively 1.10 ± 0.01 and 0.78 ± 0.01 h^{-1}) but not for E553K mutant which surprisingly showed a six times higher severing activity (3.80 ± 0.01 h^{-1}) even in the absence of Ca^{2+} (Fig. 1). Although such Ca^{2+}-independent activity is probably not high enough to be relevant in a physiological environment, it does suggest that E553K substitution compromises the compact inactive state of the protein. In the presence of Ca^{2+}, all the tested variants had high severing efficiency, similar to that of the WT protein, suggesting there is no loss-of-function associated with these GSN substitutions.

2.2. G4:G5 mutations affect both the stability and the unfolding behavior of GSN

To investigate the effects of the G4 and G5 mutations on the stability of GSN, the three variants were subjected to temperature and pressure denaturation studies following circular dichroism (CD) and tryptophan fluorescence signals, and the analysis was repeated for the two functional states of GSN, active and inactive. Both techniques showed that G4:G5 substitutions significantly destabilize the protein fold.

Although irreversible, thermal denaturation of GSN was successfully used to characterize other G2-linked pathological variants (D187N, N184K and G167R) [27–29]. In the absence of Ca^{2+}, WT GSN displays prototypical single transition behavior, consistent with the compact and nearly globular conformation of the protein (Fig. 2A). In the presence of the ion, WT GSN unwinds, many inter-domain contacts are modified or lost, and denaturation takes place through a multi-state process [27,28]. Surprisingly, all the variants also showed different qualitative behaviors, suggesting a complex role of the mutated residues. The A551P mutation led to stepwise denaturation even in the absence of Ca^{2+}, while a single transition was always observed for the E553K and M517R variants.

Because of the differences in melting patterns, to quantify the mutation-dependent destabilization we investigated the temperature of the first denaturation events (temperature of onset, T_{on}). T_{on} for mutated GSN were lower than those of WT protein (Table 1). In the absence of Ca^{2+}, ΔT_{on} (mutant-WT) is −9 °C for A551P, −13 °C for E553K, and −9 °C for M517R. The addition of Ca^{2+} had little effect on the T_{on} of WT and A551P proteins, while the extent of destabilization was conformation-specific for E553K and M517R. E553K appeared to be the most unstable of all the variants, with a T_{on} of 39.9 ± 2.3 °C in the absence of Ca^{2+} (in agreement with the actin-severing activity, Fig. 1B).

We also investigated the thermal stability of the G5 variants on the isolated domain. The A551P substitution (Fig. S2) induced only slight destabilization of the isolated domain compared to G5-WT (T_m 63.4/55.8 °C with/without Ca^{2+}), with a ΔT_m of −4.4 °C in Ca^{2+} and −5.1 °C without Ca^{2+}, while E553K substitution strongly destabilized G5-E553K, with ΔT_m, respectively, −14.0 °C and −19.3 °C compared to G5-WT.

The impact of the mutations on the stability of full-length GSN proteins was also checked by pressure-induced denaturation followed by intrinsic fluorescence emission. Besides the folding state of the individual domains, Trp fluorescence monitors the loss of inter-domain contacts and is thus informative of the conformational state of the protein. Denaturation can be modeled by a standard two-state equation with sloping baselines (Fig. 2B), a pattern already observed in chemical denaturation studies on WT and D187N/Y GSN [23], and interpreted as the result of highly dynamic folded and unfolded states. Pm and ΔV_0 (reported in Table 1), defined, respectively, as the pressure of the transition midpoint

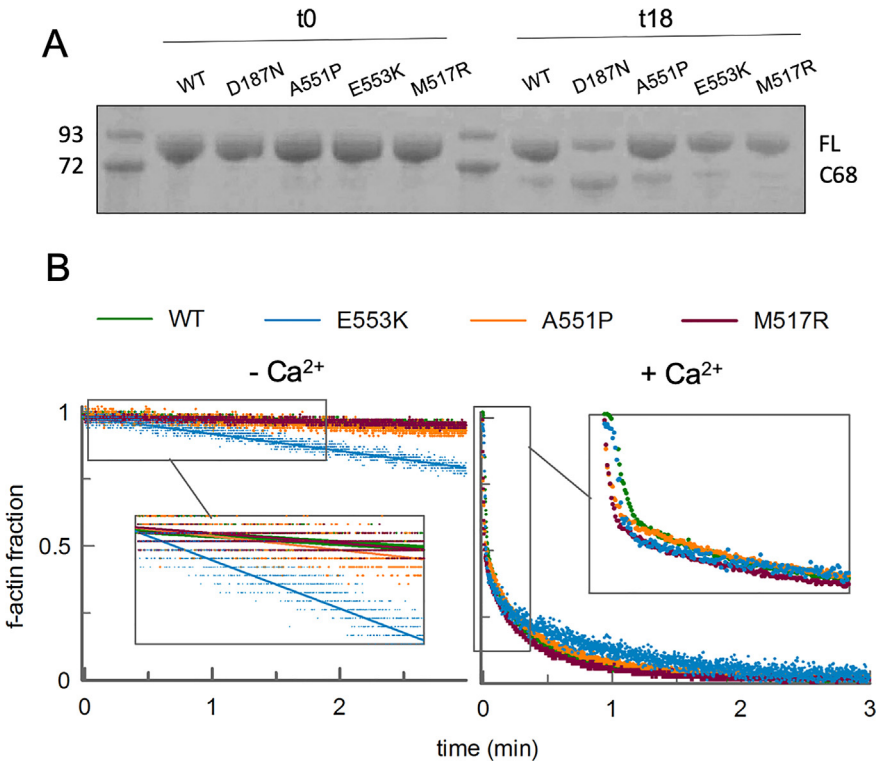

Fig. 1. Susceptibility to furin proteolysis and actin-severing activity. A. WT, D187N, A551P, E553K, M517R GSN were analyzed by SDS-PAGE before (t0) and 18 h after incubation (t18) with furin. Full-length (FL) and C68 fragment are indicated. **B.** Actin-severing activity of WT and mutated GSN was evaluated with and without saturating Ca^{2+} by measuring the fluorescence intensity of pyrene-labeled f-actin over time.

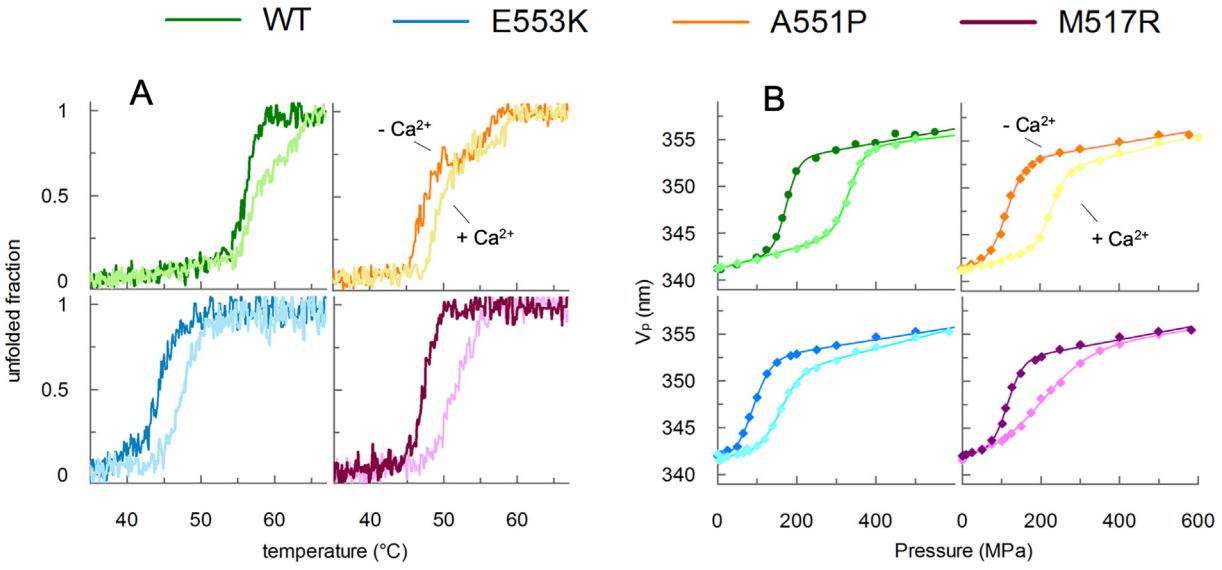

Fig. 2. Impact of the mutations on temperature and pressure stability. A. Thermal denaturation of WT GSN and A551P, E553K, and M517R variants analysed by circular dichroism spectroscopy, both without (darker tracing) and with (lighter trace) saturating Ca^{2+}. **B.** Pressure-induced denaturation at 20 °C followed by the change in tryptophan fluorescence emission (same color code). V_p is the center of spectral mass (nm) of tryptophan emission. Lines show the fit of the data with a two-state equation with sloping baselines [40].

and the volume change between folded and unfolded states, are used to quantify the mutation-dependent destabilization.

Pm showed good agreement with the thermal denaturation Ton and confirmed the stability scale: WT > A551P ≥ M517R > E553K. All the variants had a reduction of the difference in stability between the Ca^{2+} bound/unbound states compared to the WT (ΔP_m = 155 MPa), modest for A551P (ΔP_m = 115 MPa) and more pronounced for E553K and M517R (85 and 73 MPa).

Assuming similar unfolding states for all the variants and in all conditions, higher net ΔV_0 values suggest a more compact folded molecule. In fact, net ΔV_0 was higher for the globular inactive GSN (−152 mL/mol) than in its dynamic and extended Ca^{2+}-

Table 1
Stability parameters for WT and mutated GSN. Mutation-dependent destabilization was evaluated with or without Ca^{2+} in thermal denaturation experiments followed by circular dichroism in the far-UV region, and the temperature of onset of denaturation is reported (T_{on}). Protein stability was measured under the same experimental conditions, in pressure denaturation studies followed by intrinsic fluorescence at 20 °C. The pressure of midpoint denaturation (P_m) and the difference of volume of the system, unfolded-folded (ΔV_0), are tabulated. Standard errors are reported.

	T_{on} (°C)		P_m (MPa)		ΔV_0 (mL/mol)	
	$-Ca^{2+}$	$+Ca^{2+}$	$-Ca^{2+}$	$+Ca^{2+}$	$-Ca^{2+}$	$+Ca^{2+}$
WT	53.0 ± 2.7	53.8 ± 3.0	174 ± 18	333 ± 21	−152 ± 16	−118 ± 8
A551P	44.2 ± 1.8	46.4 ± 3.8	116 ± 16	226 ± 25	−109 ± 9	−125 ± 7
E553K	39.9 ± 2.3	46.8 ± 3.7	86 ± 10	157 ± 14	−103 ± 8	−91.3 ± 9
M517R	44.3 ± 3.7	49.6 ± 1.7	121 ± 16	214 ± 13	−122 ± 17	−34 ± 1

bound conformation (−119 mL/mol). In comparison with WT, all mutations caused 20–30% reduction of net ΔV_0 under Ca^{2+}-free conditions, particularly for A551P and E553K (−109 and −103 mL/mol), while the impact on this parameter in the presence of the ion is harder to interpret. In particular, M517R had a very low value (-34 mL/mol) but this was probably because of a loss of cooperativity of the process, as suggested by the gradual denaturation curve.

2.3. G4:G5 mutations give aggregation propensity to the unproteolysed full-length protein

To dissect the determinants and mechanisms underlying the pathological deposition of the A551P, E553K and M517R variants, we investigated their aggregation propensity *in vitro,* with the Thioflavin T (ThT) assay. This fluorogenic compound is specific for amyloid-like structures both as soluble prefibrillar aggregates and mature fibers and this property makes it widely used in diagnostics and kinetics studies.

The aggregation propensity of the G4:G5 variants, WT and D187N proteins, in the presence and absence of Ca^{2+}, was evaluated at 37 °C under stirring (Fig. 3). In the presence of Ca^{2+}, there was no increase of ThT signal for WT and mutated GSNs over five-day incubation. Behavior was similar in Ca^{2+}-free conditions for WT and the G2-linked D187N variant, which were already reported not to aggregate in their unproteolysed form and under near-physiological conditions [26]. In contrast, for the A551P, E553K and M517R variants there was an increase of the ThT signal indicative of their propensity to aggregate. This was particularly evident for E553K and M517R.

A sequence-based amyloigenicity analysis with Amylpred2 [41] identified several potential aggregation-prone sequences in WT GSN, in addition to the well-known amyloidogenic core in G2 [10]. Some of these sequences are close to the G4:G5 interface (Table S1), suggesting that their exposure due to fragmentation or misfolding of G4 and G5 domains may also lead to GSN deposition.

2.4. Both sequence and structure contribute to G4:G5 mutants (proteo)toxicity

We employed a *C. elegans*-based toxicity assay to characterize the proteotoxic potential of the novel G4:G5 variants *in vivo*. *C. elegans* specifically reacts to the toxic assemblies of amyloidogenic proteins, with a reduction of the function of its pharynx, defined as its *pumping rate* [42–45]. Employing this approach, we had already noted a good correlation between the mutation-induced destabilization and amyloidogenicity of isolated G2 domains [24]. Full-length proteins were administered to worms, with or without Ca^{2+} (Fig. 4A–D). In the absence of Ca^{2+} experiments were also repeated after a 5 days incubation under conditions similar to those of the aggregation experiments (Fig. 4E–F). The pumping rate of nematodes was measured 2 h and 24 h after the feeding to assess the transient and permanent toxic effects.

In the presence of Ca^{2+}, all GSN variants reduced pharyngeal activity by 13% (WT) to 37% (M517R) (Fig. 4A). The effect lasted over time except for the WT and the A551P protein, which reverted to vehicle levels 24 h after feeding (Fig. 4B). The overall toxic effect was less when the mutated proteins were given to the worms without Ca^{2+}, and the WT protein was not recognized as toxic under these conditions. Pharyngeal pumping at 2 h was reduced by 10–27%, following the same toxicity scale as in the presence of Ca^{2+} (Fig. 4C). Under this experimental condition, the A551P

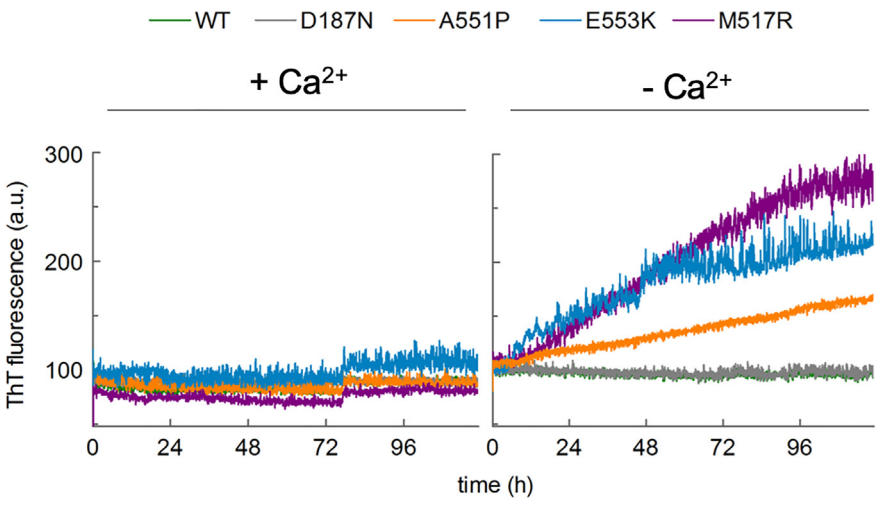

Fig. 3. Aggregation propensity of WT and mutated GSN. Propensity to form aggregates was evaluated by fluorimetric ThT assay on 10 μM GSN samples. Experiments were performed with or without saturating Ca^{2+}.

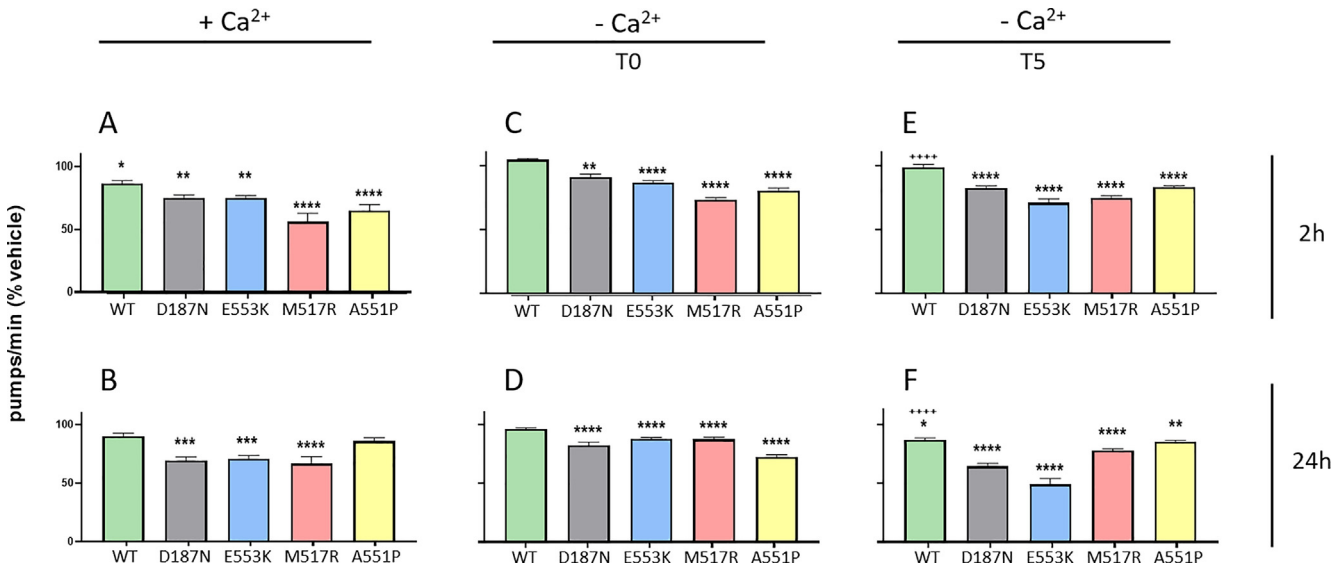

Fig. 4. ***In vivo*** **toxicity of full-length GSN is related to the protein sequence and conformation. A-D**. Proteotoxicity of GSN samples and control (vehicle) was evaluated with or without Ca^{2+}. Data are mean ± SE (N = 30/group). *p < 0.05, **p < 0.01, ***p < 0.001 and ****p < 0.0001 *vs* Vehicle, one-way ANOVA and Bonferroni *post hoc* test. **E, F.** Proteotoxicity was evaluated also after a 5-day incubation at 37 °C in the absence of Ca^{2+}. Data are mean ± SE (N = 10/group). *p < 0.05, **p < 0.005 and **** p < 0.0001 *vs* Vehicle and ++++ p < 0.0001 *vs* mutated GSN. Pharyngeal activity was determined 2 h (A, C, E) and 24 h (B, D, F) after feeding GSN variants by counting the pharyngeal bulb contractions (pumps/min).

variant became able to induce permanent dysfunction (Fig. 4D). Aging of D187N, M517R and A551P proteins resulted in a similar reduction of the pharyngeal function rated 2 h after the treatment, whereas E553K was much more toxic after the incubation (Fig. 4E). The toxicity of the aged forms of D187N, E553K and M517R, but not A551P, increased over time, indicating their strong ability to permanently affect the worms' pharyngeal function (Fig. 4F). These data suggest that the various mutations induce destabilization of the proteins over time, with different toxic properties.

Since thermal stability and time-dependent experiments showed abundant amorphous precipitation of the most destabilized variants, we also examined whether protein denaturation by flash-heating affected their proteotoxicity (Fig. S3). Denatured proteins lose their ability to impair the pharyngeal function of worms, demonstrating that *C. elegans* specifically recognizes the mutation-dependent toxicity of the folded proteins, whether in the open, closed or aggregated conformations.

2.5. The mutations affect the structure and dynamics of the G4-G5 domains

To dissect the structural determinants of the mutation-dependent destabilization, aggregation propensity and proteotoxicity we ran X-ray crystallography and molecular dynamics studies. The elusive Ca^{2+}-bound conformation of full-length GSN has never been obtained, but crystallogenesis of the Ca^{2+}-free protein is generally reproducible. All G2-linked mutants and the WT protein were previously crystallized in similar conditions, for easy comparison (same crystal lattice and similar quality of diffraction data), of atomic models [3,28,29]. Despite multiple trials, E553K and M517R proteins only grew poorly diffracting crystals, underlining once more the high destabilization of these substitutions.

Crystals of A551P in the Ca^{2+}-free conformation, instead, diffracted to 3.0 Å. The quality of the diffraction data and of the model is comparable to previously published structures (Table S2). Most of the residues belonging to the six homologous domains could be unambiguously traced in the electron density with the exception of some flexible linkers and a few stretches of G5. In this domain noisy electron density did not allow accurate placement of side chains and sufficient levels of detail for fine orientation even of the backbone, which obliged us to model a near-ideal structure similar to that of WT (Fig. S4). Analysis of the normalized B factor/residue becomes a valuable tool to quantify the increase in dynamics of the G4G5 portion of the protein (Fig. 5A). The G5 domain has greater conformational flexibility even in the WT protein. A551P substitution did not significantly increase the dynamics of the mutation site but rather that of the already flexible stretches, residues 450–460, 525–540 and 570–575.

Unrestrained explicit-solvent molecular dynamics simulations of the G4-G5 pairs (residues 412–630) were then run to explain the role of the substitutions in the destabilization of the domains. The A551P, E553K and M517R variants were subjected to triplicate runs, each 1 μs long, which is sufficient to observe mutation-induced local rearrangements but not long enough to sample large-scale conformational changes, such as those required for amyloid-like aggregation.

As a first analysis, we identified the most mobile regions of the structures, computing the fluctuation of each residue with respect to their initial position over the simulation time, plotted as B factor in Fig. 5B. In accordance with the crystallographic data, the areas of greater conformational flexibility common to all the analysed variants are the linker connecting the G4 and G5 (residues 520–530) and the 450–460 loop. Interestingly, E553K had greater flexibility also in the region between residues 540 and 550, which lies at the interface between the G4 and G5 domains. This flexibility may explain the actin severin activity, suggesting that this interface might be partially opened and bind actin. There was a strong local effect for the M517R variant, with a B factor peak corresponding to the mutation site.

To rationalize the structural impact of each point mutation we superimposed the starting protein configurations and those after 1 μs of simulation and calculated the corresponding root-mean squared distance (RMSD), equal to 1.85, 2.10, 2.30 and 2.54 Å, respectively, for the WT, A551P, E553K and M517R proteins (Fig. 6). Comparison of these RMSD for the three variants suggests increasing dynamicity of the overall G4-G5 portion, which is 13% to 37% higher than in the WT.

Both in the Ca^{2+}-bound and Ca^{2+}-free forms of WT GSN [3,7], G4 and G5 domains are paired within an interface consisting of two parallel β strands (residues 517–520 and 549–553). The two

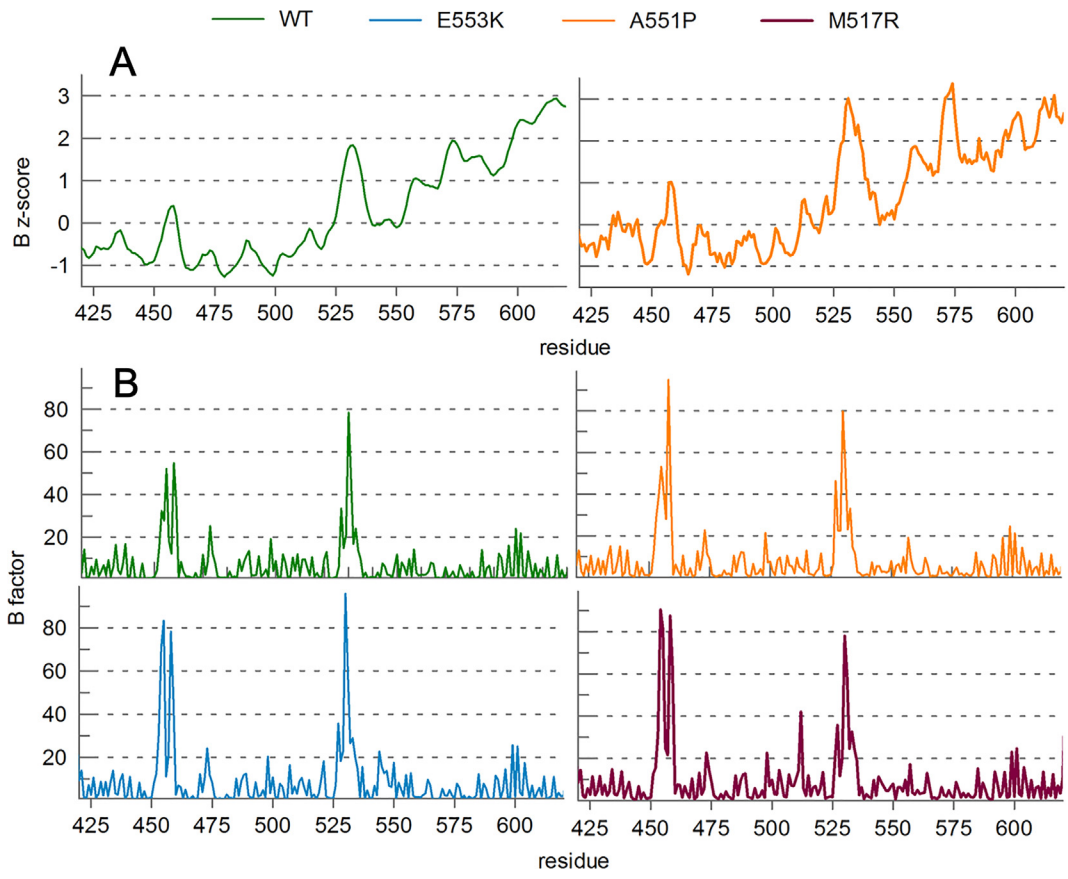

Fig. 5. Mutation-induced local conformational flexibility. A. Displacement of atoms of the backbone of the G4-G5 region are reported as the temperature factors of the atomic models from crystallographic data for the WT protein (PDB id: 3FFN [3]) and A551P (this study). Both are expressed as Wilson B-factors, normalized in the latter analysis (B z-score)**. B.** Displacement of atoms of the backbone of the G4-G5 region are reported as the fluctuations with respect to their initial position through molecular simulations of a G4-G5 construct.

domains establish tight packing through an extended H-bond network that contributes to global folding and stability of the protein. In the A551P mutant there was a loss of the planarity of both edge β-strands of G4 and G5 and of some helical portions. Proline residues are β breakers and impair strand-strand interactions [46]. The inter-strand bond between A551 and M517 was lost because the closure of amino N in a pyrrolidine ring exhausts the electronic demand for N (Fig. 6A). In the WT protein, E553 is involved in salt bridges with the guanidine of residue R537 and the amide group of K251, which confers high conformational stability (Fig. 6B). The E to K substitution caused local rearrangements due to charge repulsion, which led to increased local flexibility. M517R was the variant with the largest RMSD and showed strong destabilization of the G4:G5 interface. In the WT protein M517 extends its side chain towards a sulphur-aromatic motif (S-π, [47]) which includes residues F441, W466, M509 and F512 in the core of G4 (Fig. 6C). The M517R mutation caused important upheavals of the S-π motif, as it introduces a charged and bulky residue. In addition to the loss of the π-S bond, the long side chain of R discouraged stabilizing interactions with neighboring residues.

To support the qualitative information about the destabilization of the G4:G5 interface induced by the mutations, we ran a statistical analysis of the strength of the hydrogen bond network between the backbone of the strands at the G4:G5 interface, measuring the occupancy of each inter-strand interaction along the simulations. This analysis (details in Fig. S5) showed a loss of H-bond connectivity of the interface for the three variants, equal to −0.2, −1.19 and −1.25 bonds, respectively, for M517R, E553K and A551P.

3. Discussion

Increasing numbers of amyloidogenic variants of GSN have been identified over the years as responsible for AGel, but only those hosting the substitutions in the G2 have been so far characterized at a molecular level. Little is known about the recently identified A551P, E553K and M517R mutations hosted in the interface between G4 and G5 domains, whose aggregation very likely follows an alternative pathway. The G4:G5 interface does not harbor any putative site potentially recognized by furin (the protease is sequence-specific), nor should the mutations affect the stability of G2 or its susceptibility to proteolysis, thus representing an ideal candidate system to explore alternative amyloidogenic pathways.

After excluding the furin cleavage as the triggering factor for aggregation of the three pathological variants and any effect on the physiological activity of GSN, we focused on the intrinsic stability of the proteins, their aggregation propensity and toxicity, and drew up a structural perspective of the effect of the substitutions on the protein (summarized in Figure 7, also in comparison with the already characterized G2-linked substitutions). These findings are a step forward toward the identification of a link between mutation and clinical phenotype, which is at the moment limited partly by the absence of a proper prognostic biomarker for AGel.

The A551P variant was identified in a patient presenting, in addition to AGel, another rare amyloidosis caused by a mutant of the transthyretin protein (ATTR-V122I) [30,37]. The patient did not have any clinical signs typical of AGel and overall A551P deposition appeared to be responsible for a mild phenotype. A551P is

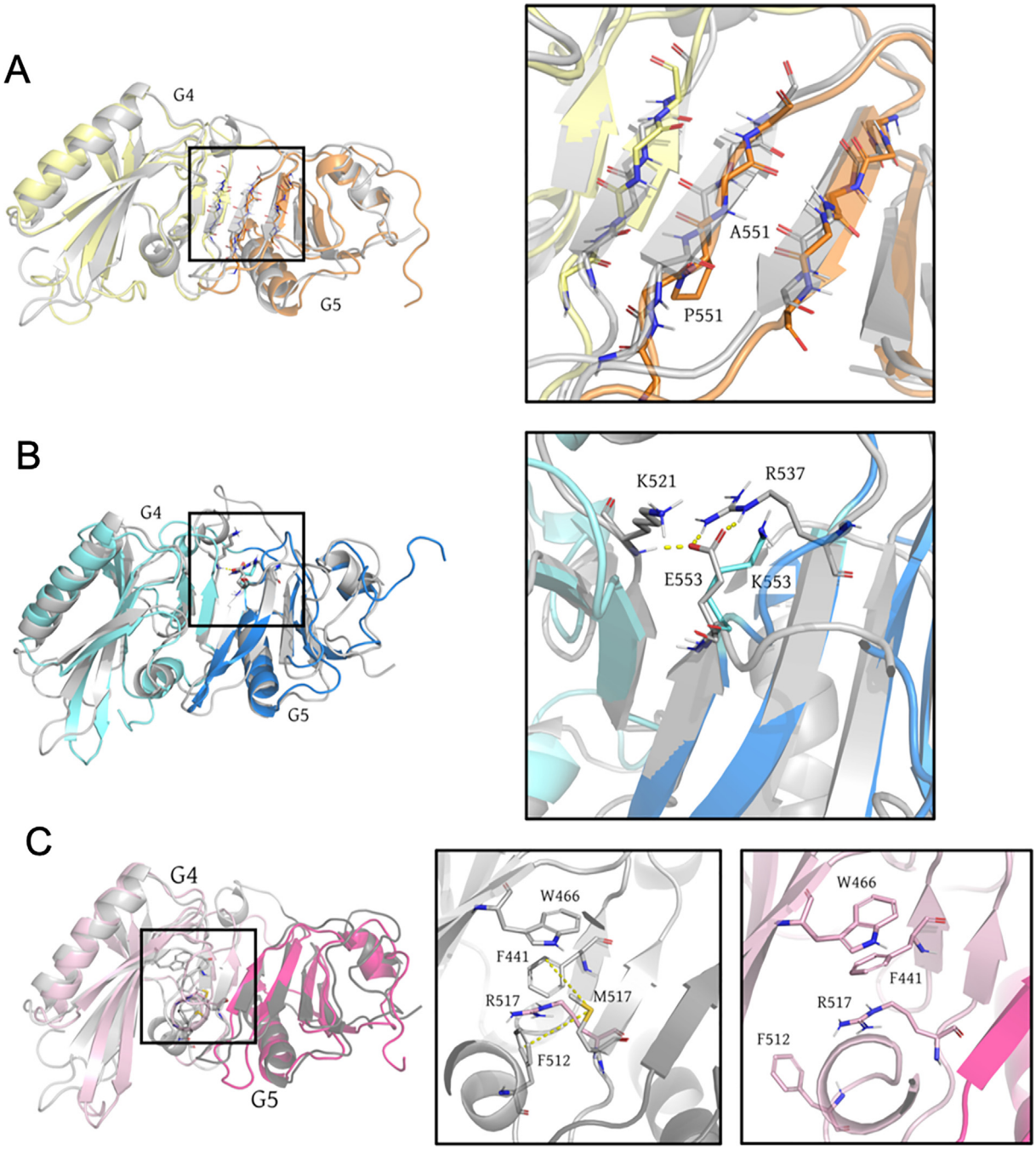

Fig. 6. Structural assessment of the impact of the G4 -G5 mutations on the interdomain arrangement of GSN. Final frames of MD simulation of (**A**) A551P, (**B**) E553K and (**C**) M517R are represented as cartoon and colored light or darker (domain G4/G5) yellow, blue and magenta, respectively, and superimposed on the final frame of the WT simulation, in grey. Images on the right show details of the respective mutation sites: mutated and interacting residues or those displaying significant displacements are shown as sticks and labeled. (For interpretation of the references to color in this figure legend, the reader is referred to the web version of this article.)

also the only G4:G5 variant whose clinical findings hint at a novel underlying molecular mechanism, since *ex vivo* analysis of the deposits identified non-canonical peptides, either products of alternative proteolytic pathways or of the deposition of the full-length protein. As expected, the impact of A551P mutation on the molecular features of GSN is mild (Fig. S6), with no large rearrangements and only modest destabilization of the protein. The A551 residue is hosted by the edge β-strand of G5, and substitution with a proline causes the loss of one H-bond and distortion of the strand itself, which loses its planarity, and weakens the connectivity of the interface (Fig. 6A and Fig. S5). Yet such minor rearrangements, in particular under Ca^{2+}-free conditions, are sufficient to disturb the overall protein architecture and metastability basins, and expose aggregation-prone stretches of the protein.

The S-π motif, of which M517 is part, appears to be a major determinant of G4 stability. The M517R substitution destroys the cluster of hydrophobic residues deep in the domain core, due to the insertion of a charged and bulky residue. As a result, M517R is the variant showing the widest flexibility spectrum (Fig. S6D), with a B factor peak in the mutation area. However, this increased conformational flexibility only results in modest destabilization, in the A551P range (Fig. S6C), as evaluated by thermal and pressure denaturations of the full-length protein. Although this mutation has a strong impact on protein structure and dynamics, the effect

is only localized and the slight destabilization of the overall architecture of the protein is likely to be only a consequence of the misfolding of the domain hosting the mutation. We observed the same mechanism for other, previously characterised, GSN mutations [24,28,38]. The M517R mutant is the one with the highest propensity to form aggregates, and also the highest transient toxicity in the *C. elegans* assay (Figure S6E–F). These findings suggest that future studies should focus on the domain hosting this mutation, looking for aggregation-prone sequences or cleavage sites of yet-to-be-identified proteases.

At the time when this manuscript was being finalised, a novel pathological variant, W466R, was identified in the same S-π motif in G4 (Fig. 6C) [49]. This variant causes a clinical phenotype similar to M517R, E553K and the classical D187N/Y mutations, including corneal lattice dystrophy, cutis laxa and peripheral neuropathy. The substitution introduces a positive charge in an otherwise hydrophobic region, suggesting a similar destabilization mechanism underlying both M517R and W466R variants.

The strongest molecular phenotype was for the E553K variant (Fig. S6), the one with the lowest thermal and pressure stability both when measured on the isolated domain and on the full-length protein, suggesting that the substitution disturbs the folding of the G5 domain and its interaction with G4. The mutated protein adopts a partially opened conformation - i.e. active and able to bind actin - even in the absence of calcium. None of the pathological variants so far characterized showed a similar behaviour [28,29] However, loss of the Ca^{2+} -dependent modulation of the actin-severing activity was obtained by engineering double to quadrupole mutations at G2 and/or G6 calcium binding sites [3]. With denaturations near to physiological conditions, it was challenging to characterize this labile variant. Abundant amorphous deposition was observed in all time course experiments but these insoluble aggregates were not toxic. The variant is also prone to form ThT-positive and toxic soluble aggregates, similarly to M517R, with which it shares a similar clinical picture, but aggravated in E553K patients also by cardiac involvement [31,32]. In the E553K protein, a basic residue replaces an acidic one in an area already crowded with positive charges, leading to intra- (G5) and inter-domain (G4:G5) charge repulsion. As a consequence, the two domains are pushed away and local connectivity is significantly impaired. There was a good correlation between propensity to aggregate and toxicity for the E553K variant, where we observed the greatest permanent impairment of pharyngeal pumping at T5. This time-dependent increase of toxicity is another unique feature of E553K, previously observed for other amyloidogenic proteins in the same *C. elegans* assay. For these better characterized systems it was correlated with the formation of toxic soluble oligomers [43,50,51]. Whether this is due to quantitative or qualitative features of the aggregates remains to be established.

In conclusion, we identified a novel hotspot of GSN instability and pathogenicity: the interface between domains G4 and G5. Another intradomain interface (G2:G3) was recently shown to be relevant for GSN amyloidogenicity [29]. Researchers were in fact able to reproduce the amyloidogenic pathway underlying the deposition of D187N/Y GSN by engineering mutations that impair the interaction between domains G2 and G3. We also demonstrated that different mechanisms of destabilization, namely strand distortion, charge repulsion and steric hindrance, can all cause local destabilization or loss of connectivity sufficient to relax the GSN global architecture (Fig. 7). The reorganization of the domains, in particular in the absence of calcium ions, that stabilize the individual domains, leads to the exposure of stretches of the protein prone to aberrant interactions. This novel mechanism of GSN pathological aggregation is proposed here to stimulate more clinical research, particularly on the chemical nature of patients' deposits. Although the larger number of diagnoses, including those caused by new variants, suggest an increased awareness of the disease, AGel is still understudied.

4. Materials & methods

4.1. Protein production

The A551P, E553K and M517R variants in the full-length gelsolin and the isolated G5 domain were produced by site-directed mutagenesis, using the WT construct as a template and the Q5® Site-Directed Mutagenesis Kit (New England BioLabs). Primers were designed using the manufacturer's software (nebasechanger.neb.com). Wild-type (WT) full-length human GSN and the three variants were expressed as heterologous proteins in E. coli cells and purified following the protocols reported in [27,28], and WT G5 domain and its A551P and E553K variants were produced using the protocols for the isolated G2 reported in [27,38]. Briefly, all the proteins were produced in E. coli SHuffle® (New England Biolabs) and expression induced upon addition of 1 mM IPTG for 16 h at 18 °C in Luria Bertani broth. After harvesting, cells were resuspended in 20 mM sodium phosphate pH 7.4, 500 mM NaCl (for isolated domain we add 10% glycerol and 20 mM imidazole), protease inhibitor cocktail (cOmplete, EDTA-free, Roche) and 10 μg/ml of Deoxyribonuclease I from bovine pancreas and 20 mM $MgSO_4$. Cells were then lysed by high pressure in a Basic Z Bench top (Constant Systems Limited, U.K.) at 25 kPSI and centrifuged at 38,700 RCF for 45′. Full-length variants were purified by affinity chromatography using a HisTrap HP column (all column materials were purchased from GE-Healthcare), followed by anion-exchange (Resource Q) and size-exclusion chromatography on a HiLoad 16/600 Superdex 200 column with buffer 20 mM HEPES pH 7.4, 100 mM NaCl, 1 mM EDTA, 1 mM EGTA. For the purification of isolated G5 variants, the affinity chromatography was followed by the cleavage of the 6xHis-tag (5 U of thrombin/mg of G5 for 1 h at room temperature) and then the sample was passed through a HiLoad 16/600 Superdex 75 column equilibrated with 20 mM HEPES pH 7.4, 100 mM NaCl, 3 mM $CaCl_2$. All proteins were concentrated to 10 mg/ml and stored at −20 °C.

4.2. Furin proteolysis assays

Furin cleavage assays were done as reported in [24] using 4 U of commercial furin enzyme (New England BioLabs Inc., Ipswich, Massachusetts, USA) and 1 mg/ml of the WT, D187N, A551P, E553K e M517R variants in 20 mM MES, pH 6.5, 100 mM NaCl, 1 mM $CaCl_2$. The final volume of each reaction mix was 60 μL. 12 μL aliquots of the reaction mix were collected right upon addition of furin (t0) and after overnight incubation at 37 °C (t18). The reaction was quenched by adding to each sample 4 μL of Sodium Dodecyl Sulphate (SDS) loading buffer (Bio-Rad Laboratories Inc., Hercules, USA) supplemented with 0.7 M β-mercaptoethanol and by incubating at 90 °C for 3 min. Proteolysis was then monitored by gel electrophoresis (Nu-PAGE precast gel, Thermofisher scientific) and blue-coomassie staining.

4.3. Fluorimetric actin severing assay

Pyrene-labeled rabbit skeletal muscle globular actin (G-actin; Cytoskeleton, Inc. (Denver, CO, USA)) was used to evaluate the severing activity of the pathological variants of gelsolin. Preparation of the solutions, actin manipulation and conversion of G-actin to filamentous actin (F-actin) were reported elsewhere [52]. Measurements were made at 20 °C with a Cary Eclipse fluorimeter (Agilent Technologies, USA), with the following settings: excitation and emission wavelength/slit, respectively, 365/5 and 407/5 nm;

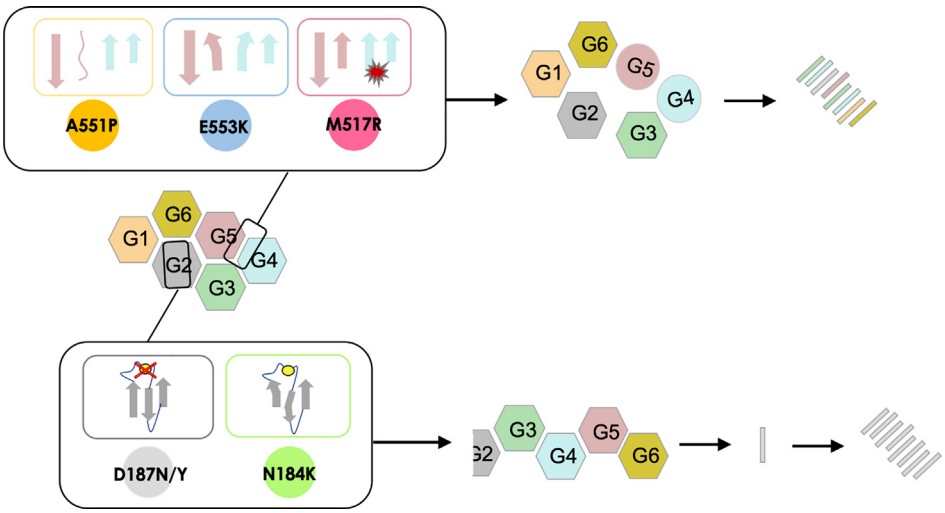

Fig. 7. Different mechanisms of destabilization may trigger alternative amyloidogenic pathways. Graphical description of the impact of mutations on the hosting domain. Previous studies showed that D187N/Y impairs Ca^{2+}-binding in G2 [23,24,48], with the ion having a structural role, whereas N184K causes similar destabilization due to a loss of connections, without affecting the capacity to bind the ion [28,38]. Both mutations lead to exposure of a proteolysis-sensitive site and trigger the canonical furin-dependent aggregation mechanism. Despite the local destabilization and susceptibility to furin proteolysis, the mechanism underlying G167R aggregation still remains to be fully elucidated [27]. The three mutations focused in this study (A551P, E553K and M517R) are not cleaved by furin, yet they disturb the interface between G4 and G5, where the substitutions cluster. Three different mechanisms of destabilization were identified: distortion of the edge strand, charge repulsion, destabilization of the G4 fold, respectively, for the A551P, E553K and M517R variant.

averaging time 0.1 s. A 3 mL cuvette was used, with a stirring bar for continuous agitation of the reaction mixture; 400 μL of a 4 μM F-actin solution were incubated in the cuvette until stabilization of the fluorescence signal, then 2 μL of 50 μM GSN were added (0.25 μM final concentration). Once the signal was stable again, the severing reaction was started by adding 2 μL of a 1 M $CaCl_2$ solution (final free Ca^{2+} concentration > 1 mM). Data were normalized based on initial and end-point fluorescence measured in the presence of Ca^{2+}. For the Ca^{2+}-free assays, measurement is started on addition of the proteins and the depolymerization rate is calculated by linear fitting over 3 min.

4.4. Denaturation monitored by circular dichroism and fluorescence emission

Thermal stability of the GSN variants was evaluated as previously reported [28]. Briefly, proteins were diluted to 0.2 mg/mL in 20 mM HEPES, pH 7.4, 100 mM NaCl and either 1 mM EDTA or 1 mM $CaCl_2$. Loss of protein secondary structures was monitored following circular dichroism at 218 nm during a 20 to 95 °C temperature ramp (1 °C/min). The temperature of onset (T_{on}) of denaturation for the full-length proteins was calculated by fitting the linear portion of the curve and at the beginning of the denaturation. For the isolated domains which showed standard two-state behavior, the melting temperature (T_m) was calculated as reported [27].

Fluorescence spectra of WT and mutant GSN were monitored at equilibrium as a function of pressure, from 0.1 to 600 MPa, at 20 °C, on a homemade apparatus using pulsed excitation (λ_{ex} 292 nm) [53]. Fluorescence emission in the spectral range 300–430 nm was monitored by a back-illuminated 1340x400 pixels CCD camera (Princeton Instruments Spec-10:400B (XTE) Roper Scientific, Trenton, NJ), cooled to −60 °C. The reversibility of the changes induced by pressure was checked at the end of each pressure cycle. Pressure effects were not promptly and completely reversible for all the proteins analyzed: after 12 h the recovery of the fluorescence characteristics was 70–80% for WT and less (about 50%) for the mutants, both without (1 mM EDTA) and with Ca^{2+} (50 mM): The delayed recovery suggests that after decompression there is slow, continuous reorganization of the loose structure. Folding/unfolding transitions of multidomain proteins are usually characterized by a few partially folded equilibrium intermediates in which folded and unfolded domains coexist [54,55]. Usually these intermediate states are produced fast, and slowly evolve to the native one [54]. At each pressure, the spectral changes in protein fluorescence emission were quantified by determining the center of spectral mass, defined as $\nu_P = (\Sigma \nu_i F_i)/F_T$) where F_i is the fluorescence intensity at the wavenumber ν_i, and F_T is the total fluorescence emitted from the protein. The fraction of unfolded protein was determined at each pressure from the displacement of ν_P [56]. Pressure unfolding was analyzed following a two-state model ($N \leftrightarrow U$) [57], implemented with sloping baseline correction [23].

4.5. Crystallization, structure solution and analysis

For crystallization trials we used an Oryx-4 nanodispenser robot (Douglas Instrument) with the sitting drop vapor-diffusion method. Experiments were carried out using A551P concentrated to 10 mg/mL (120 μM) in 20 mM HEPES, 100 mM NaCl, 1 mM EGTA, 1 mM EDTA, pH 7.4 at 20 °C. The best diffracting crystals appeared in 1.3 M ammonium sulfate, 100 mM Tris–HCl, 15% glycerol, pH 8.5. X-ray diffraction data of A551P were collected at beamline I04 at Diamond Light Source (Harwell Science and Innovation Campus in Oxfordshire). A551P data were processed using XDS [58] and scaled with AIMLESS [59]. Structures were solved by molecular replacement with PHASER [60] using the WT gelsolin crystal structure (PDB ID 3FFN [3]) as a search model. *Phenix refine* [61] was used for refinement of the structure and the manual model was built with Coot [62]. The structure of full-length A551P (two molecules in the asymmetric unit) was deposited with PDB ID 7P2B. On account of the better quality of the electron density for chain A, we used this molecule for the analyses. The structure was analysed with PyMOL (Schrödinger; DeLano 2002), which was also used to prepare the figures. B-factors were normalized (Bz-score) and analyzed as reported in [63].

4.6. Oligomerization kinetics monitored by ThT fluorescence

Aggregation kinetics were followed using an *in situ* ThT fluorescence assay based on the increase of the ThT fluorescence signal when bound to β sheet-rich structures [64]. The different variants,

at a final concentration of 10 μM, were incubated under continuous orbital shaking in 20 mM Hepes buffer pH 7.4, 100 mM NaCl and either 1 mM $CaCl_2$ or 1 mM EDTA, at 37 °C in microplate wells (Microplate Corning 3881, 96-well, low-binding, Corning Inc. Life Sciences, Acton, MA) with 20 μM ThT and 0.02% NaN_3 (100 μL solution/well). ThT fluorescence was measured every 5 min using an F500 Infinity plate reader (Tecan Italia Srl, Cernusco Sul Naviglio, Italy). The dye was excited at 448 nm, and emission was measured at 485 nm.

4.7. Proteotoxicity studies on C. elegans

The Bristol N2 strain was obtained from the *Caenorhabditis elegans* Genetic Center (CGC, University of Minnesota, Minneapolis, MN, USA) and propagated at 20 °C on solid Nematode Growth Medium (NGM) seeded with *E. coli* OP50 (CGC) for food. The effect of WT GSN and GSN carrying the D187N, A551P, E553K or M517R mutation on pharyngeal behavior was investigated as already described [24]. Briefly, worms were incubated with 1.5 μg/mL of protein (100 worms/100 μL) in 20 mM HEPES solution containing 100 mM NaCl (Hepes solution) and 1 mM $CaCl_2$ or 150 μM EDTA, pH 7.4. Hydrogen peroxide (1 mM) was administered in dark conditions as a positive control (100 worms/100 μL). Control worms were fed 20 mM HEPES solution with 1 mM $CaCl_2$, pH 7.4 (100 worms/100 μL) only.

After 2 h of orbital shaking, worms were transferred onto fresh NGM plates seeded with OP50 *E. coli*. The pharyngeal pumping rate, measured by counting the number of times the terminal bulb of the pharynx contracted over a 1-min interval (pumps/min), was scored 2 and 24 h later. In selected experiments *C. elegans* were fed 1.5 μg/mL GSN (100 μL/100 worms), previously incubated or not at 37 °C for 5 days in 20 mM Hepes solution containing 1 mM $CaCl_2$ or 150 μM EDTA. After 2 h of orbital shaking, worms were transferred onto fresh NGM plates seeded with OP50 E. coli and pharyngeal activity was determined 2 h and 24 h later, as described above.

For the experiments with the heat-denatured variants, WT, A551P and M517R proteins at 1.5 μg/mL in 20 mM Hepes solution containing 100 mM NaCl and 1 mM $CaCl_2$ before and after incubation at 100 °C for 10 min were fed to *C. elegans* (100 worms/100 μL). Control worms (100 worms/100 μL) were treated with 20 mM Hepes solution containing 100 mM NaCl and 1 mM $CaCl_2$ alone. Pharyngeal pumping was measured 2 h and 24 h after the treatment as described above.

4.8. MD simulations

Starting configurations for molecular dynamics simulations were built on the basis of the crystallographic structure of full-length WT GSN (PDB ID: 3FFN [3]), retaining residues M412 to L630 of chain A, comprising G4 and G5 domains. The truncation sites were capped with neutral acetylated and N-methylated termini. The structures of the three mutants A551P, E553K and M517R were generated *in silico* by substitution of the mutated residue. Each mutant and the WT model were parameterized with the AMBER ff14SB force field; protonation states for pH 7.4 were assigned with the ProteinPrepare algorithm [65]. The resulting system was solvated with TIP3P water in a 79 × 79 × 79 $Å^3$ box, neutralized and ionized with 150 mM NaCl. The preparation and building steps were conducted using the HTMD package [66].

Each system was energy-minimised for 500 steps with the L-BFGS algorithm, then equilibrated at 1 atm constant pressure (NPT) for 20 ns with the Berendsen thermostat. Given the relatively high stability of all of the variants, the dynamics at varying temperatures was probed with a set of exploratory runs of 1 μs each at 300 K, 325 K and 343 K, held with the Langevin thermostat.

Consistent with the thermal stability measurements, only at 343 K the simulations displayed any appreciable modulation of the local dynamics on the sampled time-scale of 1 μs. In order to gather sufficient sampling, production MD runs were carried out in triplicate for each variant and WT form at 343 K in unbiased constant-volume conditions. The 12 trajectories (4 systems × 3 replicas) were then analysed with custom Python scripts to compute donor–acceptor distances and local mean squared displacements. All the runs employed a 4 fs time step with the hydrogen mass repartitioning scheme [67] and rigid bonds, and were computed on GPU clusters with the OpenMM 7.4.1 library [68] with the MiniOMM wrapper.

Declaration of Competing Interest

The authors declare that they have no known competing financial interests or personal relationships that could have appeared to influence the work reported in this paper.

Acknowledgements

We gratefully acknowledge CINECA awards under the ISCRA initiative for the availability of high-performance computing resources and support. T.G. thanks the GPUGRID.net project participants for donating computing time. The authors would like to thank Diamond Light Source for beamtime (proposal MX20221), and the staff of beamline I04 for assistance. The work was partly supported by a grant from the amyloidosis foundation to M.d.R. We thank Prof. Louise Gourlay for critical reading the manuscript.

Appendix A. Supplementary data

Supplementary data to this article can be found online at https://doi.org/10.1016/j.csbj.2021.11.025.

References

[1] Yin HL, Stossel TP. Control of cytoplasmic actin gel–sol transformation by gelsolin, a calcium-dependent regulatory protein. Nature 1979;281(5732):583–6. https://doi.org/10.1038/281583a0.
[2] Sun HQ, Yamamoto M, Mejillano M, Yin HL. Gelsolin, a multifunctional actin regulatory protein. J Biol Chem 1999;274(47):33179–82.
[3] Nag S, Ma Q, Wang H, Chumnarnsilpa S, Lee WL, Larsson M, et al. Ca2+ binding by domain 2 plays a critical role in the activation and stabilization of gelsolin. Proc Natl Acad Sci U S A 2009;106(33):13713–8.
[4] Choe H, Burtnick LD, Mejillano M, Yin HL, Robinson RC, Choe S. The calcium activation of gelsolin: insights from the 3Å structure of the G4–G6/actin complex. J Mol Biol 2002;324(4):691–702. https://doi.org/10.1016/S0022-2836(02)01131-2.
[5] McLaughlin PJ, Gooch JT, Mannherz H-G, Weeds AG. Structure of gelsolin segment 1-actin complex and the mechanism of filament severing. Nature 1993;364(6439):685–92.
[6] Kazmirski SL, Isaacson RL, An C, Buckle A, Johnson CM, Daggett V, et al. Loss of a metal-binding site in gelsolin leads to familial amyloidosis-Finnish type. Nat Struct Biol 2002;9(2):112–6.
[7] Narayan K, Chumnarnsilpa S, Choe H, Irobi E, Urosev D, Lindberg U, et al. Activation in isolation: exposure of the actin-binding site in the C-terminal half of gelsolin does not require actin. FEBS Lett 2003;552:82–5.
[8] Meretoja J. Familial systemic paramyloidosis with lattice dystrophy of the cornea, progressive cranial neuropathy, skin changes and various internal symptoms. A previously unrecognized heritable syndrome. Ann Clin Res 1969;1:314–24.
[9] de la Chapelle A, Kere J, Sack GH, Tolvanen R, Maury CPJ. Familial amyloidosis, Finnish type: G654-–a mutation of the gelsolin gene in Finnish families and an unrelated American family. Genomics 1992;13(3):898–901.
[10] Maury CP, Nurmiaho-Lassila EL, Rossi H. Amyloid fibril formation in gelsolin-derived amyloidosis. Definition of the amyloidogenic region and evidence of accelerated amyloid formation of mutant Asn-187 and Tyr-187 gelsolin peptides. Lab Invest 1994;70:558–64.
[11] Mustonen T, Holkeri A, Holmström M, Atula S, Pakarinen S, Lehmonen L, et al. Cardiac manifestations in Finnish gelsolin amyloidosis patients. Amyloid 2021;28(3):168–72.
[12] Koskelainen S, Zhao F, Kalimo H, Baumann M, Kiuru-Enari S. Severe elastolysis in hereditary gelsolin (AGel) amyloidosis. Amyloid 2020;27(2):81–8.
[13] Schmidt E-K, Kiuru-Enari S, Atula S, Tanskanen M. Amyloid in parenchymal organs in gelsolin (AGel) amyloidosis. Amyloid 2019;26(3):118–24.

[14] Pihlamaa T, Salmi T, Suominen S, Kiuru-Enari S. Progressive cranial nerve involvement and grading of facial paralysis in gelsolin amyloidosis. Muscle Nerve 2016;53(5):762–9.
[15] Kiuru-Enari S, Keski-Oja J, Haltia M. Cutis laxa in hereditary gelsolin amyloidosis. Br J Dermatol 2005;152(2):250–7. https://doi.org/10.1111/bjd.2005.152.issue-210.1111/j.1365-2133.2004.06276.x.
[16] Kiuru-Enari S, Somer H, Seppäläinen A-M, Notkola I-L, Haltia M. Neuromuscular pathology in hereditary gelsolin amyloidosis. J Neuropathol Exp Neurol 2002;61(6):565–71. https://doi.org/10.1093/jnen/61.6.565.
[17] Pihlamaa T, Suominen S, Kiuru-Enari S, Tanskanen M. Increasing amount of amyloid are associated with the severity of clinical features in hereditary gelsolin (AGel) amyloidosis. Amyloid 2016;23(4):225–33.
[18] Solomon JP, Page LJ, Balch WE, Kelly JW. Gelsolin amyloidosis: genetics, biochemistry, pathology and possible strategies for therapeutic intervention. Crit Rev Biochem Mol Biol 2012;47(3):282–96.
[19] Sethi S, Dasari S, Amin MS, Vrana JA, Theis JD, Alexander MP, et al. Clinical, biopsy, and mass spectrometry findings of renal gelsolin amyloidosis. Kidney Int 2017;91(4):964–71.
[20] Sethi S, Theis JD, Quint P, Maierhofer W, Kurtin PJ, Dogan A, et al. Renal amyloidosis associated with a novel sequence variant of gelsolin. Am J Kidney Dis 2013;61(1):161–6.
[21] Efebera YA, Sturm A, Baack EC, Hofmeister CC, Satoskar A, Nadasdy T, et al. Novel gelsolin variant as the cause of nephrotic syndrome and renal amyloidosis in a large kindred. Amyloid 2014;21(2):110–2.
[22] Ratnaswamy G, Huff ME, Su AI, Rion S, Kelly JW. Destabilization of Ca2+-free gelsolin may not be responsible for proteolysis in Familial Amyloidosis of Finnish Type. Proc Natl Acad Sci U S A 2001;98(5):2334–9.
[23] Isaacson RL, Weeds AG, Fersht AR. Equilibria and kinetics of folding of gelsolin domain 2 and mutants involved in familial amyloidosis-Finnish type. Proc Natl Acad Sci U S A 1999;96(20):11247–52.
[24] Giorgino T, Mattioni D, Hassan A, Milani M, Mastrangelo E, Barbiroli A, et al. Nanobody interaction unveils structure, dynamics and proteotoxicity of the Finnish-type amyloidogenic gelsolin variant. Biochim Biophys Acta, Mol Basis Dis 2019;1865(3):648–60.
[25] Chen CD, Huff ME, Matteson J, Page L, Phillips R, Kelly JW, et al. Furin initiates gelsolin familial amyloidosis in the Golgi through a defect in Ca(2+) stabilization. EMBO J 2001;20:6277–87.
[26] Solomon JP, Yonemoto IT, Murray AN, Price JL, Powers ET, Balch WE, et al. The 8 and 5 kDa fragments of plasma gelsolin form amyloid fibrils by a nucleated polymerization mechanism, while the 68 kDa fragment is not amyloidogenic. Biochemistry 2009;48(48):11370–80.
[27] Bonì F, Milani M, Barbiroli A, Diomede L, Mastrangelo E, de Rosa M. Gelsolin pathogenic Gly167Arg mutation promotes domain-swap dimerization of the protein. Hum Mol Genet 2018;27(1):53–65.
[28] de Rosa M, Barbiroli A, Bonì F, Scalone E, Mattioni D, Vanoni MA, et al. The structure of N184K amyloidogenic variant of gelsolin highlights the role of the H-bond network for protein stability and aggregation properties. Eur Biophys J 2020;49(1):11–9.
[29] Zorgati H, Larsson M, Ren W, Sim AYL, Gettemans J, Grimes JM, et al. The role of gelsolin domain 3 in familial amyloidosis (Finnish type). Proc Natl Acad Sci U S A 2019;116(28):13958–63.
[30] Sridharan M, Highsmith WE, Kurtin PJ, Zimmermann MT, Theis JD, Dasari S, et al. A patient with hereditary ATTR and a novel AGel p.Ala578Pro Amyloidosis. Mayo Clin Proc 2018;93(11):1678–82.
[31] Cabral-Macias J, Garcia-Montaño LA, Pérezpeña-Díazconti M, Aguilar M-C, Garcia G, Vencedor-Meraz CI, et al. Clinical, histopathological, and in silico pathogenicity analyses in a pedigree with familial amyloidosis of the Finnish type (Meretoja syndrome) caused by a novel gelsolin mutation. Mol Vis 2020;26:345–54.
[32] Potrč M, Volk M, de Rosa M, Pižem J, Teran N, Jaklič H, et al. Clinical and histopathological features of gelsolin amyloidosis associated with a novel variant p.Glu580Lys. Int J Mol Sci 2021;22. https://doi.org/10.3390/ijms22031084.
[33] Oregel KZ, Shouse GP, Oster C, Martinez F, Wang J, Rosenzweig M, et al. Atypical presentation of gelsolin amyloidosis in a man of African descent with a novel mutation in the gelsolin gene. Am J Case Rep 2018;19:374–81.
[34] Feng X, Zhu H, Zhao T, Hou Y, Liu J. A new heterozygous G duplicate in exon1 (c.100dupG) of gelsolin gene causes Finnish gelsolin amyloidosis in a Chinese family. Brain Behav 2018;8:e01151.
[35] Jiang Y, Jiao B, Liao X, Xiao X, Liu X, Shen L. Analyses Mutations in GSN, CST3, TTR, and ITM2B Genes in Chinese Patients With Alzheimer's Disease. Front Aging Neurosci 2020;12. https://doi.org/10.3389/fnagi.2020.581524.
[36] Ida CM, Yan X, Jentoft ME, Kip NS, Scheithauer BW, Morris JM, et al. Pituicytoma with gelsolin amyloid deposition. Endocr Pathol 2013;24(3):149–55.
[37] Obici L, Merlini G. Seek and you shall find: is subclinical amyloid more common than expected? Mayo Clin Proc 2018;93(11):1546–8.
[38] Bonì F, Milani M, Porcari R, Barbiroli A, Ricagno S, de Rosa M. Molecular basis of a novel renal amyloidosis due to N184K gelsolin variant. Sci Rep 2016;6:33463.
[39] Song J, Tan H, Perry AJ, Akutsu T, Webb GI, Whisstock JC, et al. PROSPER: an integrated feature-based tool for predicting protease substrate cleavage sites. PLoS ONE 2012;7(11):e50300.
[40] Clarke J, Fersht AR. Engineered disulfide bonds as probes of the folding pathway of barnase: increasing the stability of proteins against the rate of denaturation. Biochemistry 1993;32(16):4322–9.
[41] Tsolis AC, Papandreou NC, Iconomidou VA, Hamodrakas SJ, Vorberg IM. A consensus method for the prediction of "Aggregation-Prone" peptides in Globular Proteins. PLoS ONE 2013;8(1):e54175. https://doi.org/10.1371/journal.pone.0054175.
[42] Stravalaci M, Tapella L, Beeg M, Rossi A, Joshi P, Pizzi E, et al. The anti-prion antibody 15B3 detects toxic amyloid-β oligomers. J Alzheimers Dis 2016;53(4):1485–97.
[43] Zeinolabediny Y, Caccuri F, Colombo L, Morelli F, Romeo M, Rossi A, et al. HIV-1 matrix protein p17 misfolding forms toxic amyloidogenic assemblies that induce neurocognitive disorders. Sci Rep 2017;7(1). https://doi.org/10.1038/s41598-017-10875-0.
[44] Diomede L, Romeo M, Rognoni P, Beeg M, Foray C, Ghibaudi E, et al. Cardiac light chain amyloidosis: the role of metal ions in oxidative stress and mitochondrial damage. Antioxid Redox Signal 2017;27(9):567–82.
[45] Diomede L, Rognoni P, Lavatelli F, Romeo M, del Favero E, Cantù L, et al. A Caenorhabditis elegans-based assay recognizes immunoglobulin light chains causing heart amyloidosis. Blood 2014;123(23):3543–52.
[46] Richardson JS, Richardson DC. Natural beta-sheet proteins use negative design to avoid edge-to-edge aggregation. Proc Natl Acad Sci U S A 2002;99:2754–9.
[47] Reid KSC, Lindley PF, Thornton JM. Sulphur-aromatic interactions in proteins. FEBS Lett 1985;190:209–13. https://doi.org/10.1016/0014-5793(85)81285-0.
[48] Bollati M, Scalone E, Bonì F, Mastrangelo E, Giorgino T, Milani M, et al. High-resolution crystal structure of gelsolin domain 2 in complex with the physiological calcium ion. Biochem Biophys Res Commun 2019;518(1):94–9.
[49] Mullany S, Souzeau E, Klebe S, Zhou T, Knight LSW, Qassim A, et al. A novel GSN variant outside the G2 calcium-binding domain associated with Amyloidosis of the Finnish type. Hum Mutat 2021;42(7):818–26. https://doi.org/10.1002/humu.v42.710.1002/humu.24214.
[50] Stravalaci M, Bastone A, Beeg M, Cagnotto A, Colombo L, Di Fede G, et al. Specific recognition of biologically active amyloid-β oligomers by a new surface plasmon resonance-based immunoassay and an in vivo assay in Caenorhabditis elegans. J Biol Chem 2012;287(33):27796–805. https://doi.org/10.1074/jbc.M111.334979.
[51] Romeo M, Stravalaci M, Beeg M, Rossi A, Fiordaliso F, Corbelli A, et al. Humanin specifically interacts with amyloid-β oligomers and counteracts their in vivo toxicity. J Alzheimers Dis 2017;57(3):857–71.
[52] Vitali T, Maffioli E, Tedeschi G, Vanoni MA. Properties and catalytic activities of MICAL1, the flavoenzyme involved in cytoskeleton dynamics, and modulation by its CH, LIM and C-terminal domains. Arch Biochem Biophys 2016;593:24–37.
[53] Cioni P, Gabellieri E, Marchal S, Lange R. Temperature and pressure effects on C112S azurin: volume, expansivity, and flexibility changes. Proteins 2014;82(9):1787–98.
[54] Kumar V, Chaudhuri TK. Spontaneous refolding of the large multidomain protein malate synthase G proceeds through misfolding traps. J Biol Chem 2018;293(34):13270–83.
[55] Ramsay G, Freire E. Linked thermal and solute perturbation analysis of cooperative domain interactions in proteins. Structural stability of diphtheria toxin. Biochemistry 1990;29(37):8677–83.
[56] Cioni P. Role of protein cavities on unfolding volume change and on internal dynamics under pressure. Biophys J 2006;91(9):3390–6.
[57] Tognotti D, Gabellieri E, Morelli E, Cioni P. Temperature and pressure dependence of azurin stability as monitored by tryptophan fluorescence and phosphorescence. The case of F29A mutant. Biophys Chem 2013;182:44–50.
[58] Kabsch W. XDS. Acta Crystallogr D Biol Crystallogr 2010;66(2):125–32.
[59] Evans PR, Murshudov GN. How good are my data and what is the resolution? Acta Crystallogr D Biol Crystallogr 2013;69(7):1204–14. https://doi.org/10.1107/S0907444913000061.
[60] McCoy AJ, Grosse-Kunstleve RW, Adams PD, Winn MD, Storoni LC, Read RJ. Phaser crystallographic software. J Appl Crystallogr 2007;40(4):658–74.
[61] Afonine PV, Poon BK, Read RJ, Sobolev OV, Terwilliger TC, Urzhumtsev A, et al. Real-space refinement in PHENIX for cryo-EM and crystallography. Acta Crystallogr D Struct Biol 2018;74(6):531–44.
[62] Emsley P, Lohkamp B, Scott WG, Cowtan K. Features and development of Coot. Acta Crystallogr D Biol Crystallogr 2010;66(4):486–501.
[63] de Rosa M, Barbiroli A, Giorgetti S, Mangione PP, Bolognesi M, Ricagno S, et al. Decoding the Structural Bases of D76N ß2-Microglobulin High Amyloidogenicity through Crystallography and Asn-Scan Mutagenesis. PLoS ONE 2015;10(12):e0144061.
[64] LeVine 3rd H. Thioflavine T interaction with synthetic Alzheimer's disease beta-amyloid peptides: detection of amyloid aggregation in solution. Protein Sci 1993;2:404–10.
[65] Martínez-Rosell G, Giorgino T, De Fabritiis G. PlayMolecule ProteinPrepare: a web application for protein preparation for molecular dynamics simulations. J Chem Inf Model 2017;57(7):1511–6.
[66] Doerr S, Harvey MJ, Noé F, De Fabritiis G. HTMD: high-throughput molecular dynamics for molecular discovery. J Chem Theory Comput 2016;12(4):1845–52.
[67] Hopkins CW, Le Grand S, Walker RC, Roitberg AE. Long-time-step molecular dynamics through hydrogen mass repartitioning. J Chem Theory Comput 2015;11(4):1864–74.
[68] Eastman P, Swails J, Chodera JD, McGibbon RT, Zhao Y, Beauchamp KA, et al. OpenMM 7: Rapid development of high performance algorithms for molecular dynamics. PLoS Comput Biol 2017;13(7):e1005659.